



PERGAMON

INTERNATIONAL JOURNAL OF  
**SOLIDS and  
STRUCTURES**

International Journal of Solids and Structures 36 (1999) 1823–1843

## Modeling of adaptive composites including debonding

Charles E. Seeley, Aditi Chattopadhyay\*

*Department of Mechanical and Aerospace Engineering, Arizona State University, Tempe, AZ 85287-6106, U.S.A.*

Received 6 August 1997; in revised form 2 February 1998

---

### Abstract

Debonding of piezoelectric actuators for use in composite structures can result in significant changes to the static and dynamic response. This important issue is studied in the current work. The refined higher order theory for composite laminates with embedded/surface bonded piezoelectric sensors and actuators is extended to incorporate debonding of transducers by partitioning the laminate into debonded and non-debonded regions. The stress free boundary conditions at the free surfaces are satisfied in the analytical formulation. Continuity conditions between the debonded and the nondebonded regions, which are non-trivial for the higher order theory, are formulated and implemented using a penalty approach in the finite element model. The computational model is efficient and correlation with experimental results is very good. Numerical results are presented which indicate significant changes in the natural frequencies and mode shapes due to debonded transducers. © 1998 Elsevier Science Ltd. All rights reserved.

---

### 1. Introduction

Laminated composite structures with surface bonded/embedded sensors and actuators offer great potential for static and dynamic control. Essential to designing these advanced structures are accurate and efficient mathematical modeling techniques. Imperfections, such as debonding of transducers which may occur during the life of the structure can greatly alter its characteristics and must also be carefully investigated. Several mathematical models have appeared in the literature for the analysis of beams and plates with piezoelectric sensing/actuation. These include investigations based on the classical theory (Crawley and Anderson, 1989; Lee, 1990) which is limited to the analysis of thin plates, first order Mindlin type analyses (Chandrashekara and Agarwal, 1993; Tzou and Zhong, 1993) and potentially expensive layer-wise theories (Robbins and Reddy, 1991; Lee and Saravanos, 1995). An hybrid theory has also been presented by Mitchel and Reddy (1995). It is well-known that displacement based refined higher order theories are capable of capturing the transverse shear deformation through the thickness. These theories are applicable to laminates of

---

\* Corresponding author. Fax: 001 (602) 965-1384; e-mail: aditi@asu.edu

thicker construction and have been shown to be useful for modeling adaptive composite laminates (Reddy, 1990; Chattopadhyay and Seeley, 1996). Finite element based solution procedures (Chandrashekara and Agarwal, 1993; Robbins and Reddy, 1991; Chattopadhyay and Seeley, 1996) are attractive since they can include practical geometries and boundary conditions.

A significant amount of research has also been performed in modeling defects such as delamination in composites. Although three-dimensional approaches (Yang and He, 1994; Whitcomb, 1989) are more accurate than two-dimensional theories (Pavier and Clarke, 1996; Whitcomb, 1981; Kardomateas and Schmueser, 1988; Gummadi and Hanagud, 1995), their implementation can be very expensive for practical applications. The layer-wise approach (Barbero and Reddy, 1991) is an alternative since it is capable of modeling displacement discontinuities. However, the computational effort increases with the number of plies. Recently, a refined higher order theory, developed by Chattopadhyay and Gu (1994), was shown to be both accurate and efficient for modeling delamination in composite plates and shells of moderately thick construction. This theory has also been shown to agree well with both elasticity solutions (Chattopadhyay and Gu, 1996) and experimental results (Chattopadhyay and Gu, 1996).

Relatively little attention in the literature has been paid to detailed modeling issues associated with adaptive composite structures with surface bonded/embedded piezoelectric actuators and sensors including debonding. In most of the existing work, the actuators are assumed to be perfectly embedded or bonded to the primary structure. Therefore, issues associated with debonding of actuators is avoided. However, it has recently been shown by Seeley and Chattopadhyay (1996) that the control authority of smart structures can be significantly mispredicted in the presence of debonding. Debonding can also significantly alter the static and dynamic response of composite structures (Seeley and Chattopadhyay, 1997). Therefore, in the present paper, a general framework is developed for the analysis of adaptive composite laminates including the presence of debonded actuators. The refined higher order theory is used to describe the displacement field. Therefore, the developed theory accurately estimates the transverse shear deformation which is particularly important in the analysis of thick composites. The formulation also allows for both separation and slipping of the debonded regions. The analytical model is implemented using the finite element method which allows practical geometries and boundary conditions to be modeled as well.

In the developed theory, the composite laminate is partitioned into regions representing the nondebonded zone and portions of the composite laminate both above and below the debonding. The refined theory is implemented in each region and the stress free boundary conditions are imposed at the top and bottom surfaces of the laminate as well as at the debonding interface. This allows several of the higher order functions to be identified in terms of the lower order functions. Continuity conditions are formulated between the regions. These conditions are enforced in the finite element implementation using a penalty approach. They theory can be easily generalized to include multiple piezoelectric sensors, actuators and debondings.

## 2. Analysis

### 2.1. Displacement field

The geometry of the adaptive composite laminate, including debonding, is shown in Figs 1 and 2. The general displacement field with parameters indicated in Fig. 2 is defined as follows:

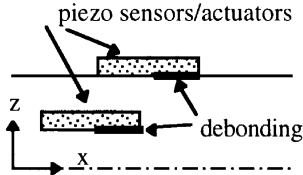


Fig. 1. Composite laminate cross section.

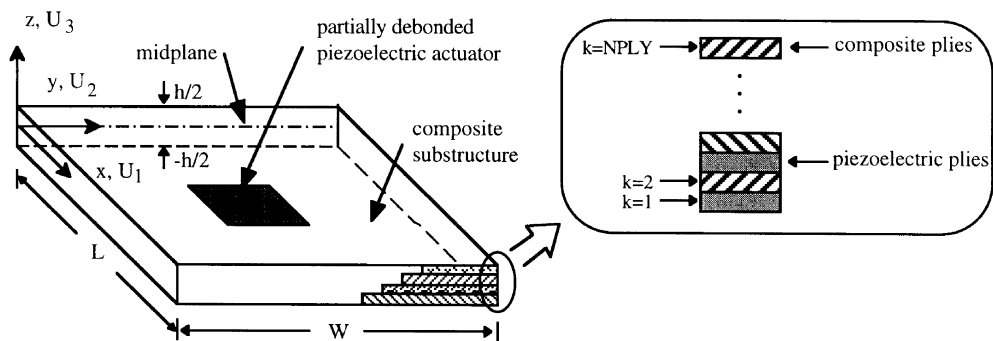


Fig. 2. Smart composite plate incorporating piezoelectric layers.

$$\begin{aligned}
 U(x, y, z) &= u(x, y) + (z - c) \left( -\frac{\partial}{\partial x} w(x, y) + \phi_x(x, y) \right) + (z - c)^2 u_2(x, y) + (z - c)^3 u_3(x, y) \\
 V(x, y, z) &= v(x, y) + (z - c) \left( -\frac{\partial}{\partial y} w(x, y) + \phi_y(x, y) \right) + (z - c)^2 v_2(x, y) + (z - c)^3 v_3(x, y) \\
 W(x, y, z) &= w(x, y)
 \end{aligned} \tag{1a–c}$$

where  $U$ ,  $V$  and  $W$  are the total displacements,  $u$ ,  $v$  and  $w$  denote the midplane displacements of a point  $(x, y)$ , the partial derivatives of  $w$  represent the rotations of normals to the midplane corresponding to the slope of the laminate and  $\phi_x$  and  $\phi_y$  represent the additional rotations due to shear deformation about the  $y$  and  $x$  axes, respectively. The quantities  $u_2$ ,  $u_3$ ,  $v_2$  and  $v_3$  represent higher order functions. This displacement field has the advantage of easily reducing to the well-known classical theory if the higher order terms are eliminated. The thickness coordinate,  $z$ , is measured from the global midplane of the laminate. Note that  $c = 0$  (Fig. 3) in the region representing the nonbonded portion of the composite.

## 2.2. Constitutive relations

The expressions relating the stress, strain, charge and electric field are derived from the electric enthalpy density function given as follows :

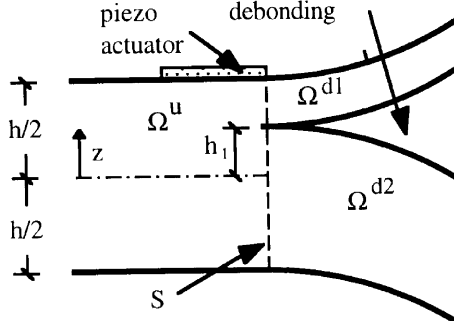


Fig. 3. Laminate cross section.

$$H(\varepsilon_{ij}, E_i) = \frac{1}{2} c_{ijkl} \varepsilon_{ij} \varepsilon_{kl} - e_{ijk} E_i \varepsilon_{jk} - \frac{1}{2} k_{ij} E_i E_j \quad (2)$$

where  $\varepsilon_{ij}$  and  $E_i$  are components of the strain tensor and electric field vector, respectively and  $c_{ijkl}$ ,  $e_{ijk}$ , and  $k_{ij}$  are the elastic, piezoelectric and dielectric permittivity constants, respectively. The stress and charge are determined as follows :

$$D_i = -\frac{\partial H}{\partial E_i} \quad (3)$$

$$\sigma_{ij} = \frac{\partial H}{\partial \varepsilon_{ij}} \quad (4)$$

For an orthotropic composite laminate with piezoelectric layers that have orthorhombic mm<sup>2</sup> symmetry in the context of laminate theory, the constitutive relationships are simplified as follows :

$$\begin{bmatrix} \sigma_1 \\ \sigma_2 \\ \sigma_3 \\ \sigma_4 \\ \sigma_5 \\ \sigma_6 \end{bmatrix}_k = \begin{bmatrix} \bar{Q}_{11} & \bar{Q}_{12} & 0 & 0 & 0 & \bar{Q}_{16} \\ \bar{Q}_{12} & \bar{Q}_{22} & 0 & 0 & 0 & \bar{Q}_{26} \\ 0 & 0 & 0 & 0 & 0 & 0 \\ 0 & 0 & 0 & \bar{Q}_{44} & \bar{Q}_{45} & 0 \\ 0 & 0 & 0 & \bar{Q}_{45} & \bar{Q}_{55} & 0 \\ \bar{Q}_{16} & \bar{Q}_{26} & 0 & 0 & 0 & \bar{Q}_{66} \end{bmatrix}_k \begin{bmatrix} \varepsilon_1 - \Lambda_1 \\ \varepsilon_2 - \Lambda_2 \\ \varepsilon_3 \\ \varepsilon_4 \\ \varepsilon_5 \\ \varepsilon_6 \end{bmatrix}_k \quad (5)$$

$$D_{3k} = [d_{31} \quad d_{32}]_k \begin{bmatrix} \bar{Q}_{11} & \bar{Q}_{21} \\ \bar{Q}_{21} & \bar{Q}_{22} \end{bmatrix}_k \begin{bmatrix} \varepsilon_1 \\ \varepsilon_2 \end{bmatrix}_k \quad (6)$$

where  $\Lambda$  are the induced strains ( $\Lambda_1 = \Lambda_2 = d_{31} E_3$ ). It is important to note that engineering normal ( $\varepsilon_{1-3}$ ) and shear ( $\varepsilon_{4-6}$ ) strains are now used in the above equations,  $\varepsilon_3$  is set to zero and only the inplane piezoelectric constants ( $d_{31}$  and  $d_{32}$ ) are retained in the context of the current work.

### 2.3. Refined displacement field

To account for the effects due to debonding, it is necessary to partition the laminate into several different regions as shown in Fig. 3. These regions include the nondebonded region  $\Omega^u$ , the region above the debonding ( $\Omega^{d1}$ ) and the region below the debonding ( $\Omega^{d2}$ ). The interface between the nondebonded region and the debonded regions, indicated by the dashed line in Fig. 3, is denoted  $S$ . The general form of the higher order displacement field [eqn (1)] is independently applied to each of these regions to describe displacements which account for slipping and separation due to the debonding. However, this displacement field does not necessarily satisfy the condition that the transverse shear stresses,  $\sigma_4$  and  $\sigma_5$ , vanish at the top and bottom surfaces of the plate ( $z \pm h/2$ ) as well as on the debonded interface surfaces ( $z = h_1$ ) in the debonded region. That is,

$$\sigma_4(x, y, \pm h/2) = 0, \quad \sigma_5(x, y, \pm h/2) = 0 \quad (7)$$

$$\begin{aligned} \sigma_4(x, y, h_1) &= 0, \quad \sigma_5(x, y, h_1) = 0 \\ (x, y) \in \Omega^r \quad (r &= u, d1, d2) \end{aligned} \quad (8)$$

in which the superscript  $r$  corresponds to either the nondebonded region ( $u$ ), or the regions above and below the debonding ( $d1$  and  $d2$ ), respectively. For orthotropic plates, these conditions are equivalent to the requirement that the corresponding strains be zero on these surfaces. A refined displacement field is obtained by applying these boundary conditions in each region as follows :

$$\begin{aligned} U_1^r &= u^r + (z - c^r) \left( -\frac{\partial w^r}{\partial x} + \phi_x^r \right) - (z - c^r)^3 \frac{4}{3(d^r)^2} \phi_x^r \\ U_2^r &= v^r + (z - c^r) \left( -\frac{\partial w^r}{\partial y} + \phi_y^r \right) - (z - c^r)^3 \frac{4}{3(d^r)^2} \phi_y^r \\ U_3^r &= w^r \quad (r = u, d1, d2) \end{aligned} \quad (9)$$

where  $c^r = [(a^r + b^r)/2]$  is the local midplane and  $d^r = b^r - a^r$  is the thickness of the region. The quantities  $a^r$  and  $b^r$  correspond to the bottom and top coordinates of the local region, respectively, as shown in Fig. 4. It is important to note that several of the higher order terms in the generalized

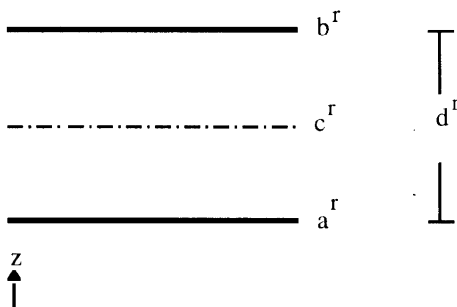


Fig. 4. Local region plate geometry.

displacement field are either found to be zero or are defined in terms of the lower order functions. The displacements [eqn (9)] in each region are defined by independent functions with parameters given as follows :

$$\begin{Bmatrix} a^r \\ b^r \end{Bmatrix} = \begin{Bmatrix} h/2 \\ -h/2 \end{Bmatrix}, \quad (x, y) \in \Omega^r, \quad r = u \quad (10a)$$

$$\begin{Bmatrix} a^r \\ b^r \end{Bmatrix} = \begin{Bmatrix} h/2 \\ h_1 \end{Bmatrix}, \quad (x, y) \in \Omega^r, \quad r = d1 \quad (10b)$$

$$\begin{Bmatrix} a^r \\ b^r \end{Bmatrix} = \begin{Bmatrix} h_1 \\ -h/2 \end{Bmatrix}, \quad (x, y) \in \Omega^r, \quad r = d2 \quad (10c)$$

In the above equations the thickness of the plate,  $h$ , may vary due to the presence of surface bonded sensors/actuators.

#### 2.4. Continuity conditions

Additional boundary conditions must be imposed to ensure the continuity of displacements at the interface of the nondebonded and the debonded regions ( $S$ ) as shown in Fig. 5. A vector of the displacements is constructed to simplify formulation of the boundary conditions as follows :

$$\mathbf{U}^r = \begin{bmatrix} U^r \\ V^r \\ W^r \end{bmatrix} \quad (r = u, d1, d2) \quad (11)$$

The continuity conditions at the interface of the nondebonded and the debonded regions are imposed as follows :

$$\mathbf{U}^u = \mathbf{U}^{d1} \quad a^{d1} < z \leq \min(b^u, b^{d1}) \quad (x, y) \in S \quad (12)$$

$$\mathbf{U}^u = \mathbf{U}^{d2} \quad \max(a^u, a^{d2}) < z \leq b^{d2} \quad (x, y) \in S \quad (13)$$

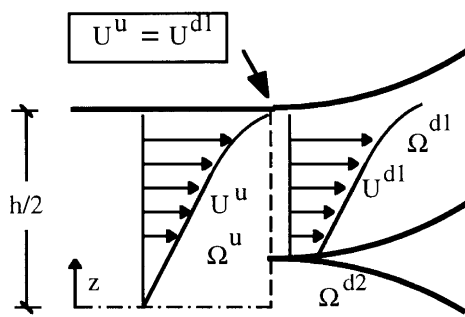


Fig. 5. Displacements in cross section.

The above equations can be exactly satisfied with the classical theory since it assumes a linear displacement distribution through the thickness. However, the displacement distribution using the refined theory is nonlinear and therefore eqns (12) and (13) can be satisfied in an average sense as follows. An error function vector for the first of the above equations is formulated as follows:

$$\mathbf{e} = \mathbf{U}^u - \mathbf{U}^{d1} \quad a^{d1} < z \leq \min(b^{d1}, b^{d2}) \quad (x, y) \in S \quad (14)$$

It is desired to minimize the difference between  $\mathbf{U}^u$  and  $\mathbf{U}^{d1}$  at each point through the thickness in  $S$ . This can be accomplished by first integrating the square of the error through the thickness as follows:

$$E = \frac{1}{2} \int_a^b (\mathbf{e}^T \mathbf{e}) dz \quad (15)$$

where  $a$  and  $b$  define the limits of integration through the thickness as indicated in the interval given in eqn (13). These integration limits must be considered carefully since the presence of surface bonded actuators/sensors may change the dimensions of the laminate in any of the regions. To satisfy the continuity conditions, it is desired to find a relationship between the independent functions in  $\Omega^u$  and  $\Omega^{d1}$  which minimizes the error in terms of the functions in the nondebonded region. Therefore, derivatives of  $E$  are taken with respect to the independent functions in  $\Omega^{d1}$  and are set to zero as follows:

$$\begin{aligned} \frac{\partial E}{\partial u^{d1}} &= \frac{\partial E}{\partial v^{d1}} = \frac{\partial E}{\partial w^{d1}} = 0 \\ \frac{\partial E}{\partial \left( \frac{\partial w^{d1}}{\partial x} \right)} &= \frac{\partial E}{\partial \left( \frac{\partial w^{d1}}{\partial y} \right)} = 0 \\ \frac{\partial E}{\partial \phi_x^{d1}} &= \frac{\partial E}{\partial \phi_y^{d1}} = 0 \end{aligned} \quad (16)$$

Taking derivative and rearranging the above equations leads to the following relationships which satisfy the continuity conditions:

$$u^r = u^u + (c^u - c^r) \frac{\partial w^u}{\partial x} + \alpha^r \phi_x^u$$

$$v^r = v^u + (c^u - c^r) \frac{\partial w^u}{\partial y} + \alpha^r \phi_y^u$$

$$w^r = w^u$$

$$\frac{\partial w^r}{\partial x} = \frac{\partial w^u}{\partial x} + \beta^r \phi^u x$$

$$\begin{aligned}\frac{\partial w^r}{\partial y} &= \frac{\partial w^u}{\partial y} + \beta^r \phi^u y \\ \phi_x^r &= \gamma^r \phi_x^u \\ \phi_y^r &= \gamma^r \phi_y^u\end{aligned}\tag{17a–g}$$

where  $r = d1$  and the above relationships correspond to regions  $\Omega^u$  and  $\Omega^{d1}$ . The exact formulation for the constants  $\alpha^r$ ,  $\beta^r$ , and  $\gamma^r$  are given in the Appendix. Identical expressions corresponding to regions  $\Omega^u$  and  $\Omega^{d2}$  are similarly formulated by setting  $r = d2$  for eqns (17a–g). It must be noted that multiple debondings can be incorporated into the developed theory by defining additional regions of debonding at arbitrary locations in the laminate.

### 3. Finite element formulation

#### 3.1. Equations of motion

The finite element method (FEM) is used to implement the refined higher order theory since it allows for the analysis of practical geometries and boundary conditions. The continuity conditions formulated in the previous section are also easily implemented using the FEM. The finite element equations are derived using the discretized form of Hamilton's principle, which is stated as follows:

$$\delta\Pi = \int_{t_1}^{t_2} \sum_{e=1}^{N_e} [\delta K^e - \delta U^e + \delta W^e] dt = 0\tag{18}$$

where  $t_1$  and  $t_2$  are the initial and the final times, respectively, and  $\delta K^e$ ,  $\delta U^e$  and  $\delta W^e$  are the element variations in the kinetic, strain and potentials energies, respectively. The finite element matrices are formulated as follows:

$$\int_{t_1}^{t_2} \sum_{e=1}^{N_e} [\delta \mathbf{w}^e \mathbf{M}^e \ddot{\mathbf{w}}^e + \delta \mathbf{w}^e \mathbf{K}^e \mathbf{w}^e - \delta \mathbf{w}^e (\mathbf{F}^e + \mathbf{F}_P^e)] = 0\tag{19}$$

where  $N_e$  is the number of elements, an overdot indicates a derivative with respect to time and the nodal degrees of freedom of each element,  $\mathbf{w}_n^e$ , are specified as follows:

$$\mathbf{w}_n^e = \begin{bmatrix} u_n & v_n & w_n & \frac{\partial w_n}{\partial x} & \frac{\partial w_n}{\partial y} & \phi_{x_n} & \phi_{y_n} \end{bmatrix}^T\tag{20}$$

Elemental nodes for the nondebonded and debonded regions are placed at the local midplanes of each region as shown in Fig. 6. The mass matrix,  $\mathbf{M}^e$ , is formulated as follows.

$$\mathbf{M}^e = \int_{A^e} \rho \mathbf{N}^{eT} \mathbf{Z} \mathbf{N}^e dA^e\tag{21}$$

where  $\rho$  is the density,  $\mathbf{N}^e$  contains the elemental shape functions and  $\mathbf{Z}$  contains the  $z$  dependence

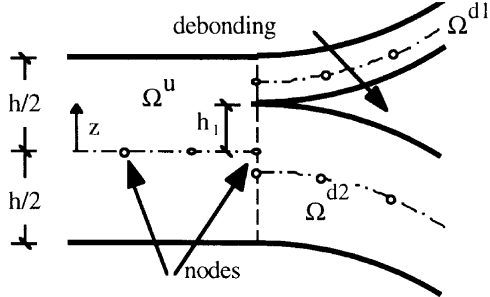


Fig. 6. Finite element discretization.

of the displacement fields. The stiffness matrix,  $\mathbf{K}^e$ , including bending and extension terms (subscript B) and transverse shear terms (subscript T) is expressed as follows :

$$\mathbf{K}^e = \int_{A^e} \mathbf{B}_B^{eT} \mathbf{A}_B \mathbf{B}_B^e dA^e + \int_{A^e} \mathbf{B}_T^{eT} \mathbf{A}_T \mathbf{B}_T^e dA^e \quad (22)$$

where  $\mathbf{A}_B$  and  $\mathbf{A}_T$  are laminate stiffness matrices and  $\mathbf{B}_B^e$  and  $\mathbf{B}_T^e$  relate the strains to the interpolated functions. Two force vectors are formulated for the distributed load ( $\mathbf{F}^e$ ) and the piezoelectric forces ( $\mathbf{F}_P^e$ ).

$$\mathbf{F}^e = \int_{A^e} \mathbf{N}_B^{eT} p^e(x, y) dA^e \quad (23)$$

$$\mathbf{F}_P^e = \int_{A^e} \mathbf{N}_B^{eT} \mathbf{A}_{B_P} \Lambda dA^e \quad (24)$$

The linear finite element equations of motion are expressed as follows :

$$\mathbf{M}\ddot{\mathbf{w}} + \mathbf{K}\mathbf{w} = \mathbf{F} + \mathbf{F}_P \quad (25)$$

where the quantities  $\mathbf{M}$ ,  $\mathbf{K}$ ,  $\mathbf{F}$  and  $\mathbf{w}$  denote the mass and stiffness matrices, the force vector due to a distributed load and the nodal displacement vector, respectively. The quantity  $\mathbf{F}_P$  is the force vector due to the piezoelectric actuation. Bilinear shape functions are used for the inplane displacements and rotations ( $u, v, \phi_x, \phi_y$ ) while a 12 term cubic polynomial is used for the transverse displacements ( $w$ ). The resulting four noded rectangular elements are nonconforming for computational efficiency and contain 28 degrees of freedom each.

### 3.2. Implementation of continuity conditions

Once the finite element model has been constructed, it is necessary to implement the continuity conditions to ensure continuity of displacements at the interface of the nondebonded and debonded regions ( $S$ ). For simplicity, consider the simple case in which the displacements in a nondebonded region,  $\Omega^u$ , must be identical to the displacements in a debonded region, and  $\Omega^d$  at the interface

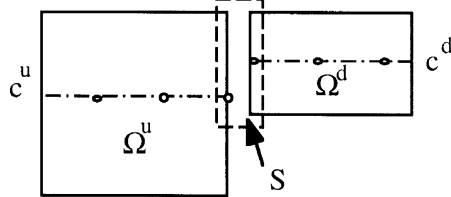


Fig. 7. Finite element discretization of debonding.

between these two regions,  $S$  (Fig. 7). Since the displacements are represented in terms of the nodal quantities in the finite element implementation, this is accomplished by applying the continuity conditions developed earlier on the unknown displacement quantities associated with the nodes contained in  $S$ . Applying these constraints directly leads to a nonsymmetric set of equations which has very undesirable consequences in the solution sequence of the finite element model. A more efficient approach needs to be developed which is outlined below.

The continuity conditions presented in eqns (17a–g), between the nondebonded  $\Omega^u$  and debonded  $\Omega^d$  regions, are applied to the finite element degrees of freedom at the interface of the nondebonded and debonded regions ( $S$ ) by first presenting these discretized conditions in matrix form as follows :

$$\tilde{\mathbf{R}}\tilde{\mathbf{w}} = \mathbf{0} \quad (26)$$

where

$$\tilde{\mathbf{w}} = [\mathbf{u}^u \quad \mathbf{u}^d]^T \quad (27)$$

$$\mathbf{u}^u = \left[ u^u \quad \phi_x^u \quad v^u \quad \phi_y^u \quad w^u \quad \frac{\partial w^u}{\partial x} \quad \frac{\partial w^u}{\partial y} \right]^T \quad (28)$$

$$\mathbf{u}^d = \left[ u^d \quad \phi_x^d \quad v^d \quad \phi_y^d \quad w^d \quad \frac{\partial w^d}{\partial x} \quad \frac{\partial w^d}{\partial y} \right]^T \quad (29)$$

and the expression for  $\tilde{\mathbf{R}}$  is presented in the Appendix. The superscripts  $u$  and  $d$  refer to the corresponding quantities in the nondebonded and debonded regions, respectively, which are also contained in  $S$ . It must be noted that to obtain eqn (26), eqns (17d–g) are multiplied by the thickness of the debonded region ( $d^d$ ) for consistency of units. Continuity of velocities must also be maintained. Therefore, eqn (26) is differentiated with respect to time to yield the following expression

$$\tilde{\mathbf{R}}\dot{\tilde{\mathbf{w}}} = \mathbf{0} \quad (30)$$

Next, the discretized potential energy is reformulated as follows :

$$V = \frac{1}{2}(-\mathbf{w}^T \mathbf{K} \mathbf{w} + \mathbf{w}^T \mathbf{F} + \mathbf{w}^T \mathbf{F}_P) - \frac{1}{2} \rho_1 \tilde{\mathbf{w}}^T \mathbf{R}^T \mathbf{R} \tilde{\mathbf{w}} \quad (31)$$

where the first term in the parentheses on the right hand side of eqn (32) corresponds to the actual potential energy while the last term corresponds to the penalty term related to the continuity

constraints which has been introduced. Minimization of this penalty term leads to the satisfaction of the continuity conditions. Similarly, the kinetic energy is reformulated as follows :

$$T = \frac{1}{2} \dot{\mathbf{w}}^T \mathbf{M} \dot{\mathbf{w}} + \frac{1}{2} \rho_2 \dot{\mathbf{w}}^T \mathbf{R}^T \mathbf{R} \dot{\mathbf{w}} \quad (32)$$

where the first term on the right hand side represents the actual kinetic energy while the second term is the penalty term related to the continuity constraints. Again, minimization of this penalty term requires that the continuity conditions be satisfied. The quantities  $\rho_1$  and  $\rho_2$  are scalar quantities which are chosen to be on the order of the 1-norm of the stiffness and mass matrices, respectively. Using Lagrange's method for a discrete system,

$$\frac{\partial}{\partial t} \left( \frac{\partial T}{\partial \dot{q}_k} \right) - \frac{\partial T}{\partial q_k} + \frac{\partial L}{\partial q_k} = Q_k^{nc} \quad (33)$$

where  $q_k$  are the generalized coordinates and  $Q_k^{nc}$  are the generalized forces, the following symmetric set of augmented equations of motion is obtained (with  $Q_k^{nc} = 0$ )

$$[\mathbf{M} + \rho_1 \mathbf{P}] \ddot{\mathbf{w}} + [\mathbf{K} + \rho_2 \mathbf{P}] \mathbf{w} = \mathbf{F} + \mathbf{F}_P \quad (34)$$

where  $\mathbf{P}$  is the penalty matrix that ensures that the continuity constraints are satisfied and it is calculated in terms of the nodes contained in  $S$  as follows :

$$\tilde{\mathbf{P}} = \tilde{\mathbf{R}}^T \tilde{\mathbf{R}} \quad (35)$$

The penalty matrix  $\tilde{\mathbf{P}}$  is then expanded to correspond to the global degrees of freedom ( $\mathbf{u}$ ) and has the following form :

$$\mathbf{P} = \begin{bmatrix} \ddots & & \\ & \mathbf{R}_{ii} & \cdots & \mathbf{R}_{ij} \\ & \vdots & & \vdots \\ & \mathbf{R}_{ji} & \cdots & \mathbf{R}_{jj} \\ & & & \ddots \end{bmatrix}. \quad (36)$$

The exact formulation for each of the above submatrices is presented in the Appendix.

## 4. Results

### 4.1. Experimental correlation

Experiments were conducted to validate the developed theory. Details of the experimental investigation can be found in a recent work by Seeley and Chattopadhyay (1997). A brief description is provided here for completeness. Composite specimens with bonded piezoelectric transducers were constructed with various debonding lengths to access the validity of the higher order theory

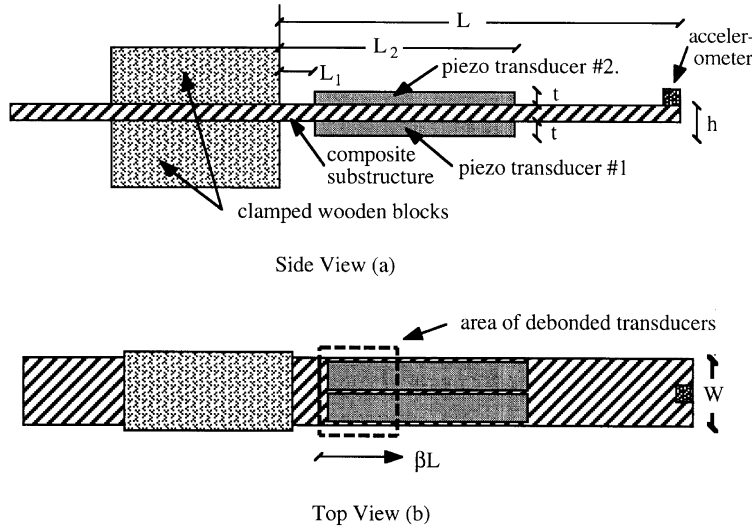


Fig. 8. Test specimen configuration.

(Fig. 8). The material selected for the composite substructure was HYE-3574 OH Graphite/Epoxy fabric. The length of the specimens was 56.3 cm and the width was  $W = 5.34$  cm. Clamped wooden blocks provided the fixed end conditions which resulted in an effective length of  $L = 30$  cm (Fig. 8) where  $L_1 = 3.4$  cm and  $L_2 = 13.7$  cm. The average thickness of the specimens was 1.94 mm and the ply thickness was approximately 0.161 mm. Active Control Experts QP40N piezoelectric transducers, which consist of two stacks of two piezoelectric wafers, with dimensions  $10.16 \times 2.54 \times 0.0762$  cm, were bonded to the upper and lower surfaces of the composite beams near the root using an Ecobond 45 clear epoxy adhesive. Material properties of the composite material and the piezoelectric transducers are presented in Table 1. Debonding was introduced at the interface between the transducer on the upper surface and the composite substructure using Teflon tape. The debonding was assumed to be through the width of the transducers with a nondimensional length of  $\beta$  where

$$\beta = \frac{L_D}{L} \quad (37)$$

Table 1  
Material properties

	$E_1$ (GPa)	$E_2$ (GPa)	$v_{12}$	$G_{12}, G_{13}$ (GPa)	$G_{23}$ (GPa)	$\rho$ ( $\times 10^3$ Kg/m $^3$ )	$d_{31}$ ( $\times 10^{-12}$ m/V)
Gr/Ep	114	9.5	0.30	4.7	2.1	1.5	—
PZT	6.9	6.9	0.31	2.6	2.6	5.0	-179

Table 2  
Natural frequencies (Hz) for Gr/Ep [0°/90°]<sub>3s</sub> beams with piezoelectric transducers

$\beta$	Mode 1			Mode 2		
	EXP	HOT	% error	EXP	HOT	% error
0	25.1	25.4	1.0	120.6	116.3	3.6
0.06	24.5	24.6	0.3	118.7	115.3	2.9
0.12	24.6	24.2	1.7	119.4	113.1	5.3
0.18	24.5	23.8	2.7	120.3	116.3	3.3

and  $L_D$  is the actual length of the debonding. Data acquisition was accomplished using a Macintosh 7200/90 computer, Labview 3.0 software and a Labview PCI 1200 I/O card. System identification was obtained using a stochastic method known as the Auto Regressive Moving Average with eXogenous input model (ARMAX) (Lee and Fassois, 1990; Mignolet et al., 1993; Mignolet and Red-Horse, 1994). A  $17 \times 3$  finite element mesh size is used for the computational model of the nondebonded laminate using the higher order theory (HOT) and additional elements are added as needed to account for varying lengths of debonding. The natural frequency estimates (HOT) and experimental results for the first two modes, which are the first and second bending modes, are presented in Table 2. Composite specimens with a stacking sequence of [0°/90°]<sub>3s</sub> and four different debonding lengths of  $\beta = 0, 0.06, 0.12, 0.18$  were studied for the experimental investigation. Correlation between the HOT and the experimental results is very good. Increasing debonding length causes the natural frequencies of the first mode to decrease as a result of reducing the stiffness of the composite structure. However, natural frequencies corresponding to the second mode actually increase for increasing debonding lengths at larger values of  $\beta$ . These nonintuitive results which are predicted by the HOT are verified experimentally and explained in greater detail in the next section. Further details of the experiments are also presented in a recent work by Seeley and Chattopadhyay (1997).

#### 4.2. Frequencies and mode shapes including debonding

The effect of debonded piezoelectric transducers on the natural frequencies and mode shapes of the composite substructure is investigated in detail next. Results are presented for composite laminates identical to the ones presented in the previous section. Again, the debonding length ( $L_D$ ) is described by the nondimensional debonding parameter  $\beta$  ( $\beta = L_D/L$ ). A  $17 \times 3$  finite element mesh size is used for the nondebonded laminate and additional elements are added as needed to account for varying lengths of debonding. The mode shapes with and without debonding of the piezoelectric transducer on the upper surface, obtained using the present approach, are presented in Figs 9 and 10 and the frequencies are shown in Table 3. The first five mode shapes in the absence of debonding are shown in Fig. 9. These mode shapes are typical of the structure being analyzed. The first two modes represent bending modes, the third and the fourth modes are twist modes and the fifth mode represents the third bending mode as indicated in the first column. The frequencies

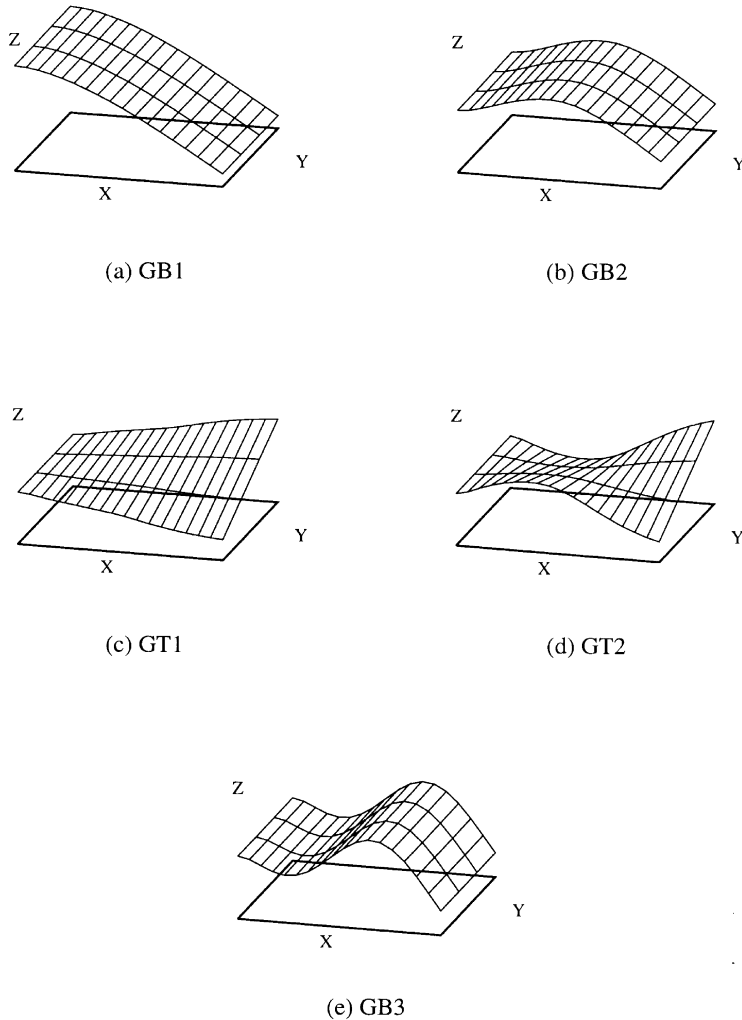


Fig. 9. (a–e) Mode shapes with no debonding obtained using the higher order theory.

corresponding to these nondebonded ( $\beta = 0$ ) modes are presented in Table 3. The sequential mode number of each of the frequencies is shown in parenthesis. As the debonding length is increased to  $\beta = 0.06$ , the magnitudes of the frequencies decrease slightly. This is due to a small reduction in the structural stiffness due to debonding. However, no significant changes are observed in the mode shapes.

Further increase in the debonding length produces significant changes in the mode shapes. The first several mode shapes for  $\beta = 0.18$  are shown in Fig. 10. It must be noted that in Fig. 10, the wire frame elements used to represent the mode shapes are plotted at the midplane of each element. The midplane corresponding to the debonded portions of the structure is different from the midplane corresponding to the nondebonded structure. Therefore, the elements in the debonded regions appear to be disconnected from the rest of the structure. This presentation of the mode

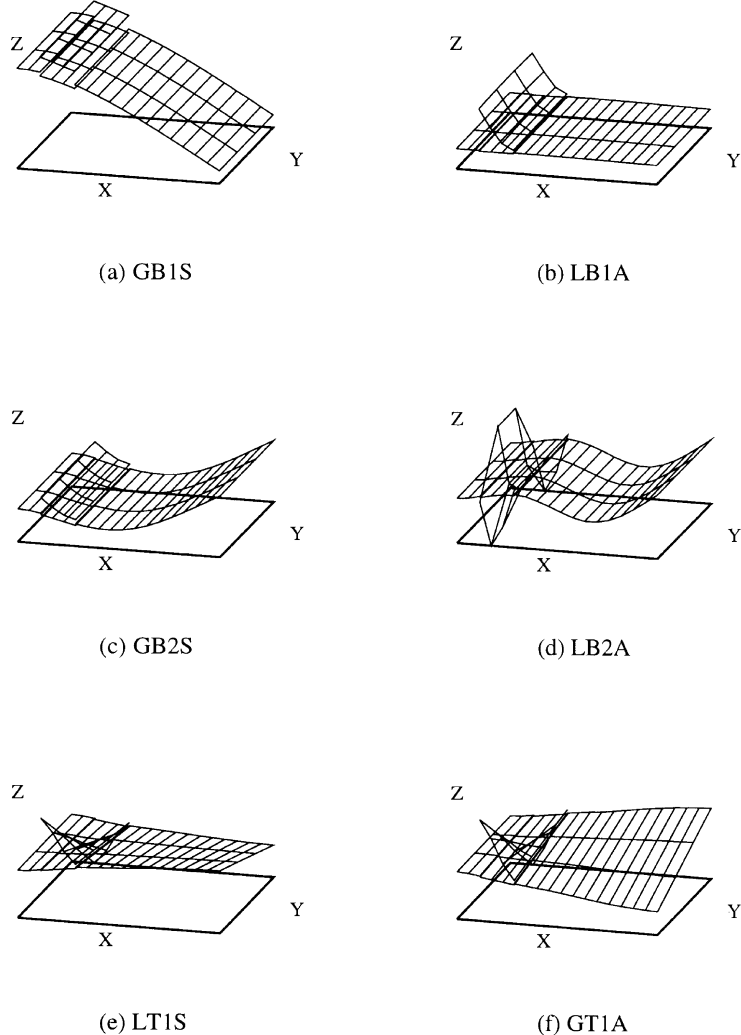


Fig. 10. (a–f) Open loop mode shapes including debonding obtained using the higher order theory.

shapes is chosen for clarity. Some of these modes, such as the first bending mode (Fig. 10(a)) exhibit global deformation of the substructure. Other modes, such as the second bending mode (Fig. 10(c)), clearly indicates local deformation caused by the debonding of the actuators. Therefore, it is necessary to study the modes with debonding in greater detail. In Table 3, frequencies corresponding to modes which exhibit bending or twisting are indicated using B or T, respectively. The letters G and L are used to indicate global or local behaviors, respectively, and S and A refer to symmetric and antisymmetric modes, respectively. For instance, Figs 10(a) and (b) show mode shapes which have characteristics of the first bending mode (B1). In Fig. 10(a), the deformation is primarily global in nature (G). However, Fig. 10(b) indicates that the deformation is predominantly local (L) due to the debonding of the actuator. The mode shape presented in Fig. 10(a) shows that

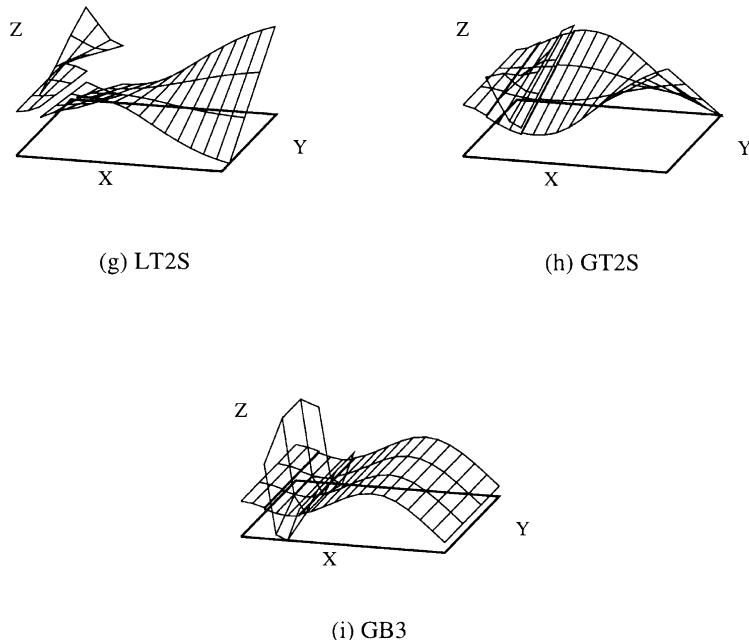


Fig. 10. (g–i) Open loop mode shapes including debonding obtained using the higher order theory.

Table 3  
Change in open loop frequencies due to debonding (Hz)<sup>a</sup>

Type	$\beta = 0.0$			$\beta = 0.06$			$\beta = 0.12$			$\beta = 0.18$		
1st bending	25.749	(1)	GB1	24.958	(1)	GB1	24.555	(1)	GB1S	24.208	(1)	GB1S
2nd bending	118.07	(2)	GB2	117.01	(2)	GB2	128.70	(3)	LB1S	55.911	(2)	LB1A
1st twist	153.28	(3)	GT1	146.26	(3)	GT1	114.85	(2)	GB2	118.12	(3)	GB2S
2nd twist							139.42	(4)	GT1S	382.29	(9)	LB2A
							222.56	(5)	LT1A	122.55	(4)	LT1S
3rd bending	311.47	(4)	GT2	299.02	(4)	GT2	266.19	(6)	LT2S	146.66	(5)	GT1A
							302.81	(7)	GT2S	275.84	(6)	LT2S
							347.48	(8)	GB3	297.55	(7)	GT2S
										327.82	(8)	GB3

<sup>a</sup>(G) global, (L) local, (B) bending, (T) twist, (S) symmetric, (A) antisymmetric.

both the deformation of the debonded region and the rest of the substructure are in phase indicating a symmetric (S) model. This is in contrast to the mode shape presented in Fig. 10(b) where the local and global deformation are out of phase indicating an antisymmetric (A) mode. Therefore, the mode shapes presented in Figs 10(a) and (b) are denoted GB1S and LB1A, respectively. The frequencies corresponding to these modes are sequential as indicated in Table 3, but their values differ significantly (24.208 Hz for LB2A and 55.911 Hz for GB2S for  $\beta = 0.18$ ).

The presence of debonding can have a significant and counter intuitive influence on the values of the frequencies corresponding to the global and local counterparts of modes displaying similar physical characteristics. It is observed that increase in the debonding length introduces local modes. For example, LB1S ( $\beta = 0.12$ ) and LB1A ( $\beta = 0.18$ ) correspond to local bending modes which are absent for smaller values of  $\beta$  (Table 3). Similar observations are made for the higher modes as well. It is also interesting to note that although there is a general decrease in the values of the natural frequencies as the debonding length is increased, the value of the frequency corresponding to the second global bending mode increases (from 114.85–118.12 Hz) as  $\beta$  is increased. Another point is that for  $\beta = 0.12$ , although the local twist modes are present (LTA1, LT2S), the second local bending mode is absent. When the second local bending mode (LB2S) does appear at  $\beta = 0.18$ , it is at a significantly higher frequency than either of the twist modes, as indicated by the magnitude of the frequency and the sequential mode number of the frequency in parenthesis. The global and local counterparts of the first twist modes for  $\beta = 0.12$  and  $\beta = 0.18$  display symmetric/antisymmetric behavior while both the global and local counterparts of the second twist modes are symmetric. These observations indicate that the dynamic characteristics of the composite laminate can be greatly altered by the presence of debonding of the piezoelectric transducers. Therefore, careful attention must be paid to the existence of such imperfections in predicting the dynamic response of such smart structures.

## 5. Concluding remarks

A general framework has been developed for the analysis of adaptive composite structures with embedded and surface bonded piezoelectric actuators and sensors in the presence of debonding. A refined third order theory has been used which accurately captures the transverse shear deformation through the thickness of the adaptive composite while satisfying the stress free boundary conditions on the free surfaces, including the debonded region. The presence of pre-existing debonding in the composite laminate at the interface between the piezoelectric actuators and the underlying substructure was studied. The results from the developed theory were correlated with experimental data. Results were also presented to demonstrate the global and local effects of debonding on the dynamics of the adaptive laminates. The following important observations were made from this study.

- (1) The developed theory provides an accurate, computationally efficient analysis tool for the study of adaptive composite laminates with piezoelectric sensing and actuation in the presence of debonding.
- (2) The theory is implemented using the finite element method to allow incorporation of practical geometries, boundary conditions and the presence of discrete piezoelectric transducers.
- (3) The developed theory correlates well with experimental results.
- (4) Debonding of the piezoelectric layer is shown to cause peeling of the actuator away from the substructure. This has important implications for failure analysis.
- (5) The length of debonding is a critical factor. Increase in debonding length introduces local and global deformations which have a significant effect on the mode shapes and frequencies.

### Acknowledgement

This research was supported by NASA Langley Research Center, Grant Number NAG-1-1648. Technical monitor, Anna McGowan.

### Appendix

The geometric parameters used in the satisfaction of the continuity conditions are given as follows:

$$\begin{aligned} \alpha^d = & (-4a^4 - 36a^3b - 60a^2b^2 - 36ab^3 - 4b^4 + 36a^2(c^u)^2 \\ & + 68ab(c^u)^2 + 36b^2(c^u)^2 + 52a^3c^d + 228a^2bc^d + 228ab^2c^d + 52b^3c^d - 72a^2c^uc^d \\ & - 136abc^uc^d - 72b^2c^uc^d - 140a(c^u)^2c^d - 140b(c^u)^2c^d - 156a^2(c^d)^2 - 388ab(c^d)^2 \\ & - 156b^2(c^d)^2 + 280ac^u(c^d)^2 + 180bc^u(c^d)^2 + 140(c^u)^2(c^d)^2 + 140a(c^d)^3 \\ & + 140b(c^d)^3 - 280c^u(c^d)^3 - 27a^2(d^u)^2 - 51ab(d^u)^2 - 27b^2(d^u)^2 \\ & + 105ac^d(d^u)^2 + 105bc^d(d^u)^2 \\ & - 105(c^d)^2(d^u)^2 / (3(9a^2 + 17ab + 9b^2 - 35ac^d - 35bc^d + 35(c^d)^2)(d^u)^2) \end{aligned} \quad (\text{A1})$$

$$\begin{aligned} \beta^d = & (18a^2 + 34ab + 18b^2 - 35ac^u - 35bc^u - 35ac^d - 35bc^d + 70c^u(c^d)(d^d)^2) / (2(9a^2 + 17ab + 9b^2 \\ & - 35ac^d - 35bc^d + 35(c^d)^2)(d^u)^2) \end{aligned} \quad (\text{A2})$$

$$\begin{aligned} \gamma^d = & (-30a^3c^u - 110a^2bc^u - 110ab^2c^u - 30b^3c^u \\ & + 72a^2c^{u2} + 136ab(c^u)^2 + 72b^2(c^u)^2 + 30a^3c^d + 110a^2bc^d + 110ab^2c^d \\ & + 30b^3c^d + 56a^2c^uc^d + 168abc^uc^d + 56b^2c^uc^d - 280a(c^u)^2c^d - 280b(c^u)^2c^d \\ & - 128a^2(c^d)^2 - 304ab(c^d)^2 - 128b^2(c^d)^2 + 140ac^u(c^d)^2 + 140bc^u(c^d)^2 \\ & + 280(c^u)^2(c^d)^2 + 140a(c^d)^3 + 140b(c^d)^3 - 280c^u(c^d)^3 - 18a^2(d^u)^2 \\ & - 34ab(d^u)^2 - 18b^2(d^u)^2 + 70ac^d(d^u)^2 + 70bc^d(d^u)^2 \\ & - 70c^{d2}(d^u)^2 + 18a^2(d^d)^2 + 34ab(d^d)^2 + 18b^2(d^d)^2 - 35ac^u(d^d)^2 \\ & - 35bc^u(d^d)^2 - 35ac^d(d^d)^2 - 35bc^d(d^d)^2 + 70c^u(c^d)(d^d)^2) / \\ & (2(9a^2 + 17ab + 9b^2 - 35ac^d - 35bc^d + 35(c^d)^2)(d^u)^2) \end{aligned} \quad (\text{A3})$$

The exact formulation of the matrices used in the penalty approach to satisfy the continuity conditions are as follows:

$$\tilde{\mathbf{R}} = \begin{bmatrix} 1 & \alpha^r & 0 & 0 & 0 & c' & 0 & -1 & 0 & 0 & 0 & 0 & 0 & 0 \\ 0 & d^r \gamma^r & 0 & 0 & 0 & 0 & 0 & 0 & -d^r & 0 & 0 & 0 & 0 & 0 \\ 0 & 0 & 1 & \alpha^r & 0 & 0 & c' & 0 & 0 & -1 & 0 & 0 & 0 & 0 \\ 0 & 0 & 0 & d^r \gamma^r & 0 & 0 & 0 & 0 & 0 & 0 & -d^r & 0 & 0 & 0 \\ 0 & 0 & 0 & 0 & 1 & 0 & 0 & 0 & 0 & 0 & 0 & -1 & 0 & 0 \\ 0 & d^r \beta^r & 0 & 0 & 0 & d^r & 0 & 0 & 0 & 0 & 0 & 0 & -d^r & 0 \\ 0 & 0 & 0 & d^r \beta^r & 0 & 0 & d^r & 0 & 0 & 0 & 0 & 0 & 0 & -d^r \end{bmatrix} \quad (\text{A4})$$

$$\mathbf{R}_{ii} = \begin{bmatrix} 1 & \alpha^r & 0 & 0 & 0 & c' & 0 \\ \alpha^r + d^r(\beta^r + \gamma^r) & 0 & 0 & 0 & \alpha^r c' + \beta^r d^r & 0 \\ 1 & \alpha_j & 0 & 0 & 0 & c' \\ & \alpha^r + d^r(\beta^r + \gamma^r) & 0 & 0 & \alpha^r c' + \beta^r d^r & 0 \\ & 1 & 0 & 0 & 0 & 0 \\ \text{sym} & & & & c'^2 + d'^2 & 0 \\ & & & & & c'^2 + d'^2 \end{bmatrix} \quad (\text{A5})$$

$$\mathbf{R}_{jj} = \begin{bmatrix} 1 & 0 & 0 & 0 & 0 & 0 \\ d^{r^2} & 0 & 0 & 0 & 0 & 0 \\ 1 & 0 & 0 & 0 & 0 & 0 \\ & d^{r^2} & 0 & 0 & 0 & 0 \\ & 1 & 0 & 0 & 0 & 0 \\ \text{sym} & & d^{r^2} & 0 & & \\ & & & d^{r^2} & & \end{bmatrix} \quad (\text{A6})$$

$$\mathbf{R}_{ij} = \begin{bmatrix} -1 & 0 & 0 & 0 & 0 & 0 & 0 \\ -\alpha^r & -\gamma^r d^{r^2} & 0 & 0 & 0 & -\beta^r d^{r^2} & 0 \\ 0 & 0 & -1 & 0 & 0 & 0 & 0 \\ 0 & 0 & -\alpha^r & -\gamma^r d^{r^2} & 0 & 0 & -\beta^r d^{r^2} \\ 0 & 0 & 0 & 0 & -1 & 0 & 0 \\ -c' & 0 & 0 & 0 & 0 & -d^{r^2} & 0 \\ 0 & 0 & -c' & 0 & 0 & 0 & -d^{r^2} \end{bmatrix} \quad (\text{A7})$$

$$\mathbf{R}_{ji} = \mathbf{R}_{ij}^T \quad (\text{A8})$$

where  $c' = c^u - c^r$ .

## References

- Barbero, E.J., Reddy, J.N., 1991. Modeling of delamination in composite laminates using a layer-wise plate theory. International Journal of Solids and Structures 28 (3), 373–388.

- Chandrashekara, K., Agarwal, A.N., 1993. Active vibration control of laminated composite plates using piezoelectric devices: a finite element approach. *Journal of Intelligent Material Systems and Structures* 4, 496–508.
- Chattopadhyay, A., Gu, H., 1994. A new higher-order plate theory in modeling delamination buckling of composite laminates. *AIAA Journal* 32 (8), 1709–1718.
- Chattopadhyay, A., Gu, H., 1996. An experimental investigation of delamination buckling and postbuckling of composite laminates. Proceedings of the ASME International Mechanical Engineering Congress and Exposition. Atlanta, GA, 7–22 November.
- Chattopadhyay, A., Gu, H., 1996. Elasticity solution for delamination buckling of composite plates. Proceedings of the 37th AIAA/ASME/ASCE/AHS/ASC Structures, Structural Dynamics and Materials Conference. Salt Lake City, UT, 15–18 April.
- Chattopadhyay, A., Seeley, C.E., 1996. A higher order theory for modeling composite laminates with induced strain actuators. *Composites Part B: Engineering*, accepted for publication.
- Chattopadhyay, A., Seeley, C.E., 1997. Experimental investigation of composites with piezoelectric actuation and debonding. Proceedings of the International Mechanical Engineering Congress and Exposition Winter Annual Meeting of the ASME: Adaptive Structures and Material Systems Symposium. Dallas, TX, 16–21 November.
- Crawley, E.F., Anderson, E.H., 1989. Detailed models of piezoelectric actuation of beams. Proceedings of the 30th AIAA/ASME/ASCE/AHS/ASC Structures, Structural Dynamics and Materials Conference. Mobile, Al., April, pp. 2000–2010.
- Gummadi, L.N.B., Hanagud, S., 1995. Vibration characteristics of beams with multiple delaminations. Proceedings of the 36th AIAA/ASME/ASCE/AHS/ASC Structures, Structural Dynamics and Materials Conference—Adaptive Structures Forum. New Orleans, LA, 10–14 April, pp. 140–150.
- Kardomateas, G.A., Schmueser, M., 1988. Buckling and postbuckling of delaminated composites under compressive loads including transverse shear effects. *AIAA Journal* 26 (3), 337–343.
- Lee, C.K., 1990. Theory of laminated piezoelectric plates for the design of distributed sensors/actuators. Part 1: Governing equations and reciprocal relationships. *Journal of the Acoustical Society of America* 87 (3), 1144–1158.
- Lee, J.E., Fassois, S.D., 1990. A stochastic suboptimum maximum likelihood approach to structural dynamics identification. Proceedings of the 8th International Model Analysis Conference. Kissimmee, FL, 29 January–1 February, pp. 1424–1433.
- Lee, H.J., Saravanos, D.A., 1995. Coupled layerwise analysis of thermopiezoelectric smart composite beams. *AIAA Journal*, submitted.
- Mignolet, M.P., Red-Horse, J.R., 1994. ARMAX identification of vibrating structures: model and model order estimation. Proceedings of the 35th AIAA/ASME/ASCE/AHS/ASC Structures, Structural Dynamics and Materials Conference—Adaptive Structures Forum. Hilton Head, SC, 21–22 April, pp. 1628–1637.
- Mignolet, M.P., Red-Horse, J.R., Lin, C.-C., 1993. A multistage ARMAX identification of structures. Proceedings of the 34th AIAA/ASME/ASCE/AHS/ASC Structures, Structural Dynamics and Materials Conference. La Jolla, CA, 19–22 April, pp. 3366–3374.
- Mitchell, J.A., Reddy, J.N., 1995. A refined hybrid plate theory for composite laminates with piezoelectric laminae. *International Journal of Solids and Structures* 32 (16), 2345–2367.
- Pavier, M.J., Clarke, M.P., 1996. A specialized composite plate element for problems of delamination buckling and growth. *Composite Structures* 35, 45–53.
- Reddy, J.N., 1990. A general non-linear third-order theory of plates with moderate thickness. *International Journal of Non-Linear Mechanics* 25 (6), 677–686.
- Robbins, D.H., Reddy, J.N., 1991. Analysis of piezoelectrically actuated beams using a layerwise displacement theory. *Computers and Structures* 41 (2), 265–279.
- Seeley, C.E., Chattopadhyay, A., 1996. Modeling delaminations in smart composite laminates. Proceedings of the 37th AIAA/ASME/ASCE/AHS/ASC Structures, Structural Dynamics and Materials Conference—Adaptive Structures Forum. Salt Lake City, UT, 15–19 April, pp. 109–119.
- Seeley, C.E., Chattopadhyay, A., 1997. Modeling of smart composite laminates including debonding: a finite element approach. Proceedings of the 38th AIAA/ASME/ASCE/AHS/ASC Structures, Structural Dynamics and Materials Conference—Adaptive Structures Forum. Kissimmee, FL, 7–11 April.
- Tzou, H.S., Zhong, J.P., 1993. Electromechanics and vibrations of piezoelectric shell distributed systems. *Journal of Dynamic Systems, Measurements and Control* 115, 506–517.

- Wang, J., Lin, C., 1995. Vibration of beam-plates having multiple delaminations. Proceedings of the 36th AIAA/ASME/ASCE/AHS/ASC Structures, Structural Dynamics and Materials Conference—Adaptive Structures Forum. New Orleans, LA, 10–14 April.
- Whitcomb, J.D., 1981. Finite element analysis of instability related delamination growth. *Journal of Composite Materials* 15, 403–426.
- Whitcomb, J.D., 1989. Three-dimensional analysis of a postbuckled embedded delamination. *Journal of Composite Materials* 23, 862–889.
- Yang, H.T.Y., He, C.C., 1994. Three-dimensional finite element analysis of free edge stresses and delamination of composite laminates. *Journal of Composite Materials* 28 (15), 1394–1412.